Beyond the bifurcation scenarios in vertical-cavity surface-emitting lasers with optical injection

Ramírez-Ávila, Gonzalo Marcelo; Carletti, Timoteo

Published in:
Chaos

DOI:
10.1063/5.0239988

Publication date:
2025

Document Version
Peer reviewed version

Chaos
An Interdisciplinary Journal
of Nonlinear Science

AIP Publishing

Beyond the bifurcation scenarios in vertical-cavity surface-emitting lasers with optical injection

Gonzalo Marcelo Ramírez-Ávila[1, 2, a)] and Timoteo Carletti[1]
[1)]*Namur Institute for Complex Systems (naXys), Université de Namur, Rue de Bruxelles 61, B-5000 Namur, Belgium*
[2)]*Instituto de Investigaciones Físicas, and Planetario Max Schreier, Universidad Mayor de San Andrés, Campus Universitario, C. 27 s/n Cota-Cota, 0000 La Paz, Bolivia*

We study the dynamic behavior in a vertical-cavity surface-emitting laser (VCSEL) subject to orthogonal optical injection through the computation of Lyapunov exponents and isospikes for a wide range of intervals in the plane of the injection parameters, i.e., the frequency detuning vs. injection strength plane. Our thorough numerical experiments on this plane constitute a deep quantitative analysis of the different bifurcation scenarios leading to polarization switching (PS). Firstly, we obtain similar results for the linearly polarized (LP) intensities for the different PS scenarios, especially when the injection strength is increased. It allows us to determine the parameter values that will be used for further analysis of the bifurcation scenarios in the parameter space. Analysis of different phase diagrams enables us to show multistability in the system and identify in the parameter planes several regions such as the predominantly chaotic lobe ones inside them are embedded some mainly regular structures such as spirals, rings, tricorns, shrimp networks, "eye(s) of chaos" and chiral and nonchiral distribution of periodicities characterized by sequences of quint points. We emphasize two routes to chaos, namely period-doubling and quint-point-based bifurcations.

Keywords: Dynamics of nonlinear optical systems, optical instabilities, laser theory, numerical simulations of chaotic systems, multistability

Lasers represent highly appealing dynamical systems because of their rich and complex behaviors, as demonstrated in the various bifurcation scenarios that we can study. These range from variations in one of the dynamical variables as a function of a parameter to computations of the largest Lyapunov exponent and isospikes. Parameter planes extend the concept of a bifurcation diagram by enabling the evaluation and control of dynamical behavior when two parameters vary simultaneously. This allows us to assess both the bifurcation features and the multistable nature of these systems. Our approach also facilitates the analysis of polarization switching and bifurcation contexts, which give rise to several dynamical structures in the parameter plane, such as period-adding shrimp sequences, rings, and other closed structures, intertwined shrimp networks, and sequences of quint points unfolding or not chirality as signatures of the route to chaos. This work aims to provide further insight into laser dynamics, enhancing our understanding of their characterization and control, which is crucial for the advancement of their technological applications.

I. INTRODUCTION

Nonlinear dynamics is at the root of numerous (if not every) natural phenomena, and it might be used to describe systems of different natures going from physics to biology or social sciences, to mention a few. The description of nonlinear dynamical systems deserved a lot of work by studying their representation in the phase space, among which the most well-known in continuous-time systems are those due to Lorenz[42] and Rössler who introduced the concept of strange attractor[63], and Chua[14] working with electronic circuits. On the other hand, in discrete-time systems, perhaps the most studied attractor corresponds to the one proposed by Hénon[35]. These studies led to the description of several types of bifurcation, starting with the one obtained by May for the logistic map[47]. An extension of the one-parameter bifurcation diagrams is the so-called parameter planes where two parameters are varying simultaneously; in this way, more details of the dynamical behavior can be captured and allow visualization of the sequences of structures describing regular behavior such as the "swallows"[51] or "shrimps"[19]. Many works have been devoted to dissecting these structures and describing the multiple ways in which they tend to be ordered in discrete[20] and continuous systems[11]. The shape of these structures describing regular behavior and their arrangements embedded in a kind of chaotic sea permit a deeper knowledge of the involved dynamical system whose characterization appears by using different tools, such as the computation of the eigenvalues[33] or the trace[58] of the Jacobian matrix, a kind of empirical method establishing a measure of stability[43], the largest Lyapunov exponent (LLE)[11], the Rényi entropy of second order in recurrence plots[80], network based methods as those involving recurrence[78] or ordinal pattern transition networks (OPTNs)[79], the fast Lyapunov indicator OFLI^2_{TT} [3], and the computation of periodicities and isospikes[18]. The shrimps organize in diverse manners into the parameter space giving rise, among others, to period-adding sequences as those found firstly in[8] when studying an optically injected semiconductor laser, and they are also very common in forced systems as in unidirectionally coupled FitzHugh–Nagumo neurons[12]; or the spiral organization discovered in the dynamics of a resistive circuit[10] and also described in several other systems[21]; and other struc-

[a)]gonzalo-marcelo.ramirezavila@unamur.be

tures such as isoperiodic rings, detected for the first time in the dynamics of a CO_2 laser[9]. These structures and some others are extensively discussed in Sect. III.

Since the invention of the first semiconductor laser[32], there has been a marked evolution in the aspects related to their functioning and applications in diverse fields. Among the variety of semiconductor lasers, the vertical-cavity surface-emitting laser (VCSEL) designed in Japan at the end of the seventies has experienced a huge development and according to Iga[36], it is possible to identify three stages in the history of VCSELs: (i) original idea and first demonstrations[68,74], (ii) first room-temperature continuous-wave (CW) device using GaAs material[39], and (iii) massive production and diversity of applications that are amply described in specialized books on VCSELs[37,50,75]. Other historical aspects of VCSELs are mentioned by Towe et al.[70]. Among the vast number of current VCSELs' applications, it is noteworthy to mention those related to computer vision, data communication, 3D sensing, LIDARs, etc. stated recently in detail[53].

Despite the astonishing applications and development of semiconductor lasers in general and VCSELs in particular, their study has also been significant from a modeling viewpoint. One of the first modeling works on lasers was about the period-doubling route to chaos in a semiconductor laser with optical injection[67] and the combination of more intense numerical work and experiments; it has been possible to identify vast chaotic and higher-order periodicity regions in the codimension bifurcation diagram frequency detuning vs injection coupling[38]. A notable advance in the description of VCSEL was the formulation of the so-called spin-flop model (SFM)[64], which constituted a basis for explaining and predicting experimental results under different circumstances. Thus, aspects such as the polarization of a VCSEL and its relationship with linear anisotropies[13,16,71] or related to the mode competition between transverse modes as a result of the frequency-dependent gain and dispersion[46]. Polarization plays an important role in VCSELs, and its control is an important aspect[52]. A phenomenon amply studied in VCSELs is polarization switching (PS), which consists of an abrupt change of the laser-emitted light in its polarization state and might be caused by mechanical[57], thermal[56], current injection[2] and optical factors, among others. Panojotov and Franco give a detailed explanation of all the factors causing polarization and their underlying dynamics[55]. Optical injection is one of the most studied aspects affecting the VCSEL dynamics and is expressed by the effects on its polarization features, output power, and wavelength. Basically, optical injection is a technique in which light from an external "master" laser source is injected into the "slave" VCSEL. Several works on this topic of semiconductor lasers subjected to optical injection are related to the experimental and computational results of the subsequent nonlinear dynamics, such as the induction of bistability polarization[54], the description of PS[27,28,34,66,69], the polarization synchronization[65], the emergence of bursting dynamics[49], and the findings of chaotic[72] and hyperchaotic[5] dynamics for light polarization.

Recently, several works have been done using LLE-based parameter planes (PPs) for the dynamical description of different types of lasers, such as in a loss-modulated CO_2 laser[11] in which superextreme events were predicted[6]; it is noteworthy to mention that a VCSEL was used in experiments of an optically injected semiconductor laser related to the discovery of extreme events in semiconductor lasers, as described by Bonatto et al.[7]; and as stated above, LLE-based PPs were also used in the description of hyperchaos in a laser diode[5]. Similarly, in a model that emulates a semiconductor laser[24] and in a free-running VCSEL[30,31] where phase stability diagrams and chiral structures were determined using PPs based on isospikes. This work deals with the in-depth study of the PPs of a VCSEL subjected to optical coupling, considering as the coordinates of the PPs the frequency detuning between the external light coming from a "master" source and the free-running VCSEL light ($\Delta\omega$), and the optical injection (E_{inj}).

The work is organized as follows. In Sect. II, we introduce the model and its main features, as well as the methods used to obtain the results stated and discussed in Sect. III, where we give the details of our findings on multistability, lobe regions, rings and other multishrimp structures, and quint points. Finally, we wrap up and conclude in Sect. IV.

II. MODEL AND METHODS

Mathematical models can significantly enhance our understanding of lasers by enabling a deep exploration of the underlying dynamics, determining key parameters, and assessing their impact on the dynamical behavior of the lasers. The dynamics of a vertical-cavity surface-emitting laser (VCSEL) subject to orthogonal optical injection involves a master laser injecting a linearly polarized (LP) light field orthogonal to the polarization of the free-running VCSEL, which acts as a slave laser.

As stated in[29], a Hopf bifurcation in the solution with two polarization modes determines the injection-locking boundaries and influences the optical injection-induced PS. To study the dynamics of a VCSEL, including the bifurcation arising from time-periodic dynamics in the two linearly polarized (LP) modes, we computed the LLEs and the number of isospikes for specific regions of the parameter space where bifurcations and PS occur. We use the same model as in[29], with the equations given in Eqs. (1):

$$\begin{aligned}
\frac{\mathrm{d}E_x}{\mathrm{d}t} =& \kappa(1+i\alpha)(NE_x + inE_y - E_x) - i(\gamma_p + \Delta\omega)E_x \\
& - \gamma_a E_x \\
\frac{\mathrm{d}E_y}{\mathrm{d}t} =& \kappa(1+i\alpha)(NE_y - inE_x - E_y) + i(\gamma_p - \Delta\omega)E_y \\
& + \gamma_a E_y + \kappa_{\text{inj}} E_{\text{inj}} \\
\frac{\mathrm{d}N}{\mathrm{d}t} =& -\gamma_e \left[N\left(1 + |E_x|^2 + |E_y|^2\right)\right] + \gamma_e \mu \\
& - i\gamma_e n \left(E_y E_x^* - E_x E_y^*\right) \\
\frac{\mathrm{d}n}{\mathrm{d}t} =& -\gamma_s n - \gamma_e n \left(|E_x|^2 + |E_y|^2\right) \\
& - i\gamma_e N \left(E_y E_x^* - E_x E_y^*\right) \quad .
\end{aligned} \tag{1}$$

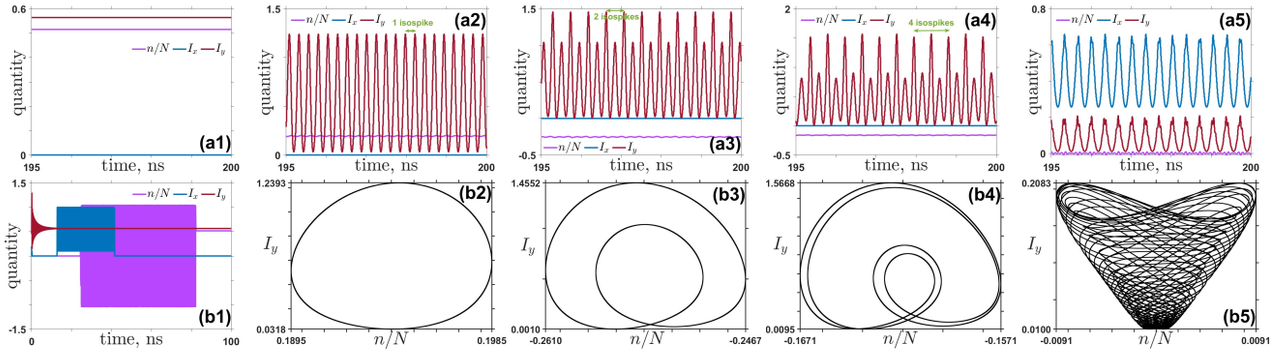

Figure 1. **First row:** Time series after a transient of 195 ns for the dynamic quantities describing the VCSEL, i.e. n/N, I_x and I_y for the parameter values stated in Table I with initial conditions $E_{xR}(0) = 0.2$, $E_{xI}(0) = 0.4$, $E_{yR}(0) = 0.3$, $E_{yI}(0) = 0.6$, $N(0) = 1.05$, and $n(0) = 0.05$ and $(\Delta\omega, E_{\text{inj}})$ values for the PP points shown in Fig. 2(a) and (b): (a1) $(0.04, 4 \times 10^9)$, (a2) $(0.04, 20 \times 10^9)$, (a3) $(0.04, 30 \times 10^9)$, (a4) $(0.04, 34 \times 10^9)$, and (a5) $(0.01, 40 \times 10^9)$. **Second row:** (b1) complete time series of (a1) that exhibit the different transients of the considered variables. (b2)–(b5) Attractors corresponding to the panels above, that is, limit cycles with (b2) one, (b3) two, and (b4) four isospikes and (b5) a chaotic attractor.

The variables E_x and E_y represent the complex electric field amplitude or the slowly varying components of the linearly polarized electric fields in the x- and y-polarization directions; we set $i = \sqrt{-1}$ and denote the complex conjugate variable with *. The variable N accounts for the total population inversion between the conduction and valence bands, while the variable n accounts for the difference in the number of carriers of the two sublevels with opposite spins. The parameters are defined as follows: κ is the optical field decay rate, γ_e the decay rate of N, γ_s the spin-flip relaxation rate, γ_α the linear dichroism, γ_p the linear birefringence, α is the linewidth enhancement factor, and μ the normalized injection current ($\mu = 1$ at threshold). External optical injection is modeled through the coupling coefficient κ_{inj}, the injected field amplitude E_{inj}, and $\Delta\omega$, which accounts for the frequency detuning between the master and slave frequencies. The free-running laser may exhibit two frequencies corresponding to those of the two linearly polarized modes. In the stationary case, the frequencies of the two LP modes are given by $\omega_{x,y} = \mp\gamma_p \pm \alpha\gamma_\alpha$. Frequency detuning is the mismatch between the master frequency ω_{inj} and a frequency ω_{th} intermediate between that of the x- and y-LP modes $\omega_{\text{th}} = \frac{\omega_x + \omega_y}{2}$, that is, $\Delta\omega = \omega_{\text{inj}} - \omega_{\text{th}}$. The intensities in the x and y directions are given by $I_{x,y} = |E_{x,y}|^2$.

A theoretical investigation has been performed in a VCSEL subject to orthogonal optical injection in[27], in which a free-running VCSEL that emits in the x-LP mode is subject to optical injection from a master laser with a y-LP polarization. An adequate selection of the model parameters permits a first insight into the polarization characteristics in the experiment of Pan et al.[54], using as bifurcation parameters the frequency detuning $\Delta\omega$ and the injected optical power $P_{\text{inj}} = |E_{\text{inj}}|^2$. A complete bifurcation diagram on the phase diagram $(E_{\text{inj}}, \Delta\omega)$ has been obtained in[29], which constitutes a basis for our numerical approach using Lyapunov exponents as a global measure of the system dynamics and isospikes as a measure of each of the dynamical variables. We consider the same parameters $(E_{\text{inj}}, \Delta\omega)$ for determining the parameter planes because both the optical injection and frequency detuning are experimentally accessible in semiconductor lasers in general[40] and VCSELs in particular[16]. The analysis of the obtained phase diagram allows us to identify some typical structures, such as individual shrimps or the organization of multiple shrimp, which give rise to more intricate structures, which are widely studied in Sect. III.

Returning to the model proposed in Eqs. (1), it is possible to rewrite it by using the real and imaginary part of the involved variables, $E_x = E_{xR} + iE_{xI}$ and $E_y = E_{yR} + iE_{yI}$, more precisely, after a straightforward algebra, we obtain the equivalent system, involving only real variables and parameters:

$$
\begin{aligned}
\frac{\mathrm{d}E_{xR}}{\mathrm{d}t} =& \left[\kappa(N-1) - \gamma_a\right] E_{xR} - \left[\kappa\alpha(N-1) - \gamma_p - \Delta\omega\right] E_{xI} \\
& - \kappa\alpha n E_{yR} - \kappa n E_{yI} \\
\frac{\mathrm{d}E_{xI}}{\mathrm{d}t} =& \left[\kappa\alpha(N-1) - \gamma_p - \Delta\omega\right] E_{xR} + \left[\kappa(N-1) - \gamma_a\right] E_{xI} \\
& + \kappa n E_{yR} - \kappa\alpha n E_{yI} \\
\frac{\mathrm{d}E_{yR}}{\mathrm{d}t} =& \kappa\alpha n E_{xR} + \kappa n E_{xI} + \left[\kappa(N-1) + \gamma_a\right] E_{yR} \\
& - \left[\kappa\alpha(N-1) + \gamma_p - \Delta\omega\right] E_{yI} + \kappa_{\text{inj}} E_{\text{inj}} \\
\frac{\mathrm{d}E_{yI}}{\mathrm{d}t} =& -\kappa n E_{xR} + \kappa\alpha n E_{xI} + \left[\kappa\alpha(N-1) + \gamma_p - \Delta\omega\right] E_{yR} \\
& + \left[\kappa(N-1) + \gamma_a\right] E_{yI} \\
\frac{\mathrm{d}N}{\mathrm{d}t} =& -\gamma_e \Big[N\left(1 + |E_x|^2 + |E_y|^2\right) - \mu \\
& - 2n\left(E_{xR}E_{yI} - E_{xI}E_{yR}\right) \Big] \\
\frac{\mathrm{d}n}{\mathrm{d}t} =& -\gamma_s n - \gamma_e n\left(|E_x|^2 + |E_y|^2\right) \\
& + 2\gamma_e N\left(E_{xR}E_{yI} - E_{xI}E_{yR}\right) \quad .
\end{aligned}
\tag{2}
$$

It is important to note, as mentioned above, that $I_x = |E_x|^2$

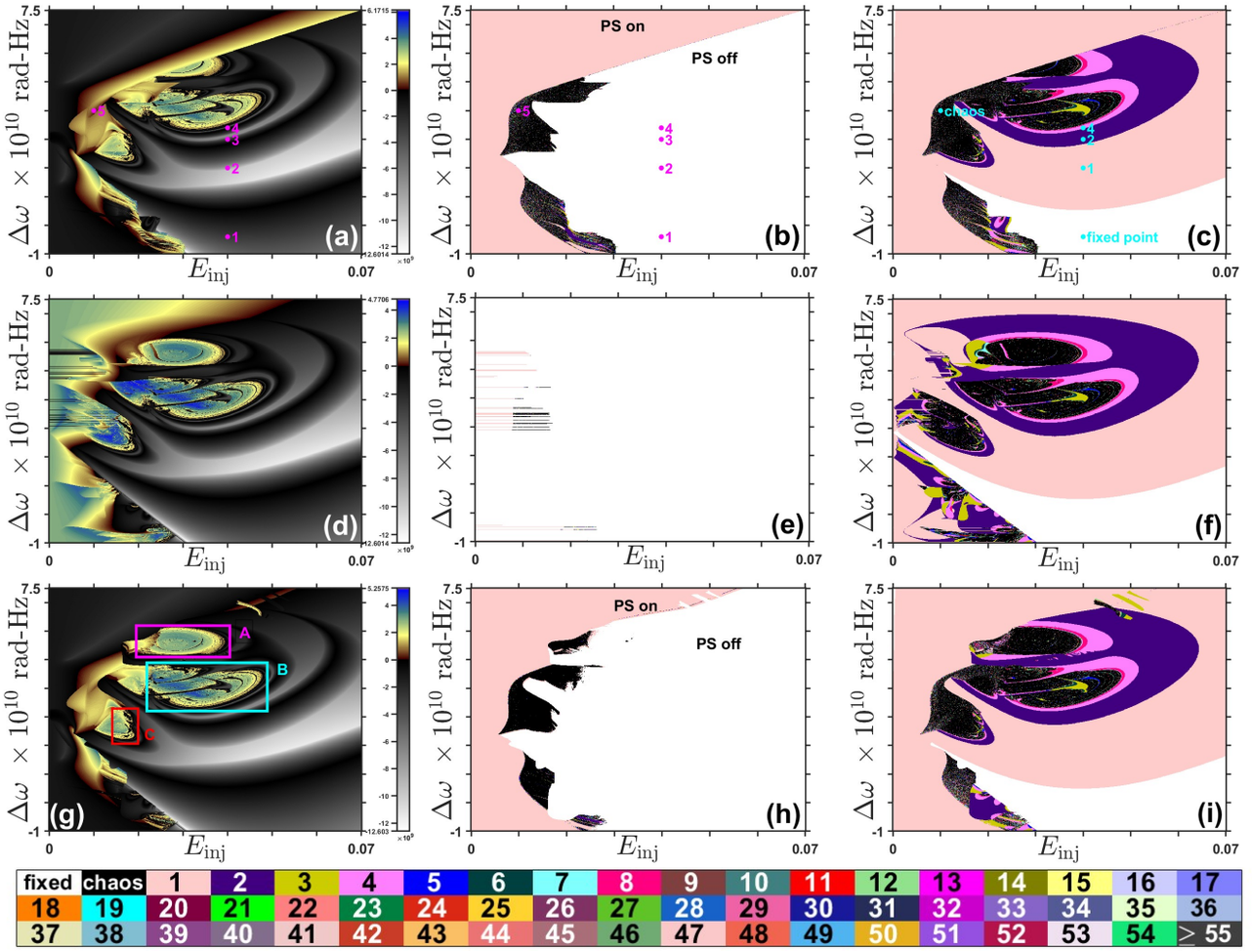

Figure 2. Parameter planes (PPs) ($\Delta\omega$ vs $E_{\rm inj}$) obtained by continuation increasing $E_{\rm inj}$ (first row) and decreasing $E_{\rm inj}$ (second row) and increasing $E_{\rm inj}$ keeping constant the initial conditions (third row). The panels (a), (d) and (g) represent the PPs based on the largest Lyapunov exponents (LLEs) for the whole system (with a color code identifying the LLEs' values, where colored and black and white regions stand for positive and negative LLEs, respectively); while the other PPs are based on the number of isospikes for I_x ((b), (e) and (h)), and for I_y ((c), (f) and (i)). The color code identifying the number of isospikes is shown at the bottom. The PPs were obtained using the parameter values stated in Table I. Note that in (a), (c), (d), (f), (g), and (i), in a global view, the regular regions are predominant and they display several branches, giving rise to lobe structures where regular and chaotic regions are intermingled. We framed two regions, A and B, that will be analyzed in Sect. III 2. The points used in Fig. 1 are marked in Figs. 2(b)–(c). Each panel displays a resolution of 1024×1024 pixels.

linewidth enhancement factor	normalized injection current	linear dichroism	decay rate of N	linear birefringence	spin-flip relaxation rate	coupling coefficient
α	μ	γ_a	γ_e	γ_p	γ_s	$\kappa_{\rm inj}$
3.0	1.5	0.5 ns^{-1}	1.0 ns^{-1}	30 rad-ns^{-1}	50 ns^{-1}	300 ns^{-1}

Table I. Mostly used parameter values.

and $I_y = |E_y|^2$ are the intensities in the x and the y direction, respectively. The previous system has been numerically integrated using the fourth-order Runge-Kutta method a time step $\Delta t = 1.0$ ps, in general, the integration time has been taken as $t = 2 \times 10^5 \times \Delta t$, and the transient as $t/2$. The values of the remaining parameters can be found in Table I.

Throughout the work, we mostly used the following initial conditions: $E_{xR}(0) = 0.2$, $E_{xI}(0) = 0.4$, $E_{yR}(0) = 0.3$, $E_{yI}(0) = 0.6$, $N(0) = 1.05$, and $n(0) = 0.05$ which are of the same order as those used in other works[30], which are characterized by being small; however, in certain situations, we use random initial conditions. Concerning the interval of values of the parameters $(E_{\rm inj}, \Delta\omega)$ used for the analysis of the parameter plane (PP), we considered those used currently in the literature, and in particular in the codimension-two bifurcation diagrams shown in[29]. Our more in-depth study of

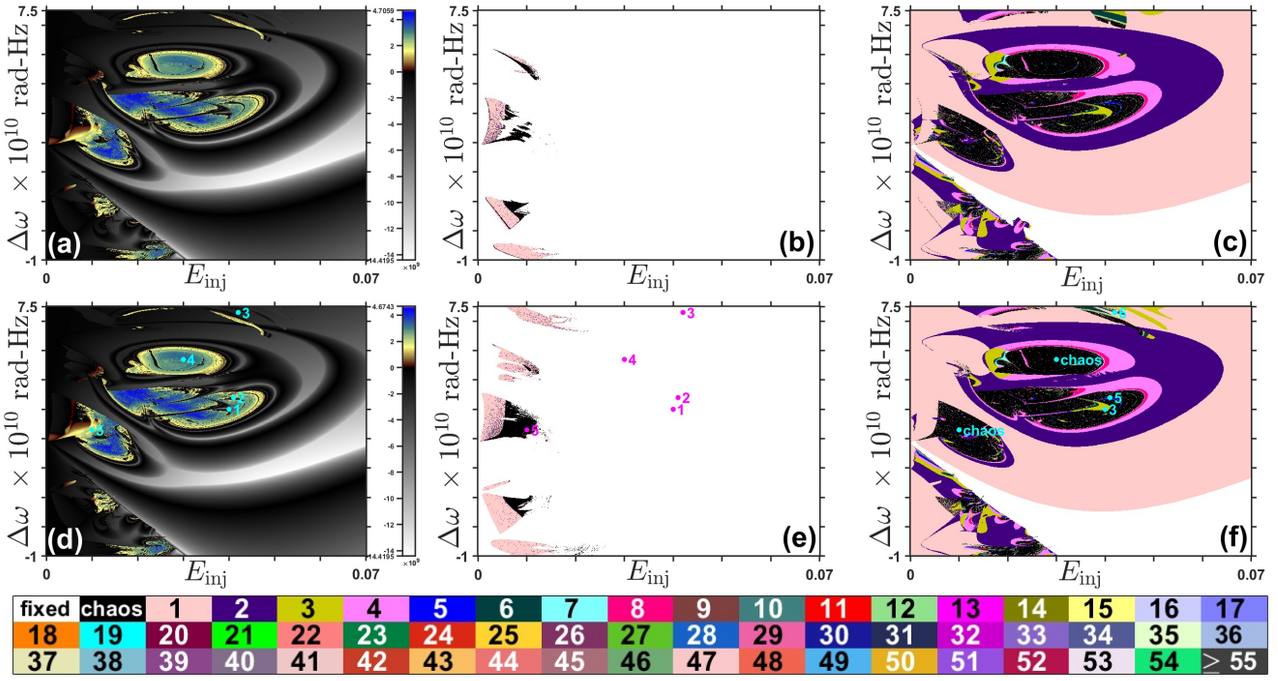

Figure 3. Parameter planes (PPs) ($\Delta\omega$ vs $E_{\rm inj}$) obtained by increasing $E_{\rm inj}$ with (first row) random and (second row) fixed initial conditions The panels (a) and (d) are PPs based on the LLEs for the whole system (with a color code identifying the LLEs' values, where colored and black and white regions stand for positive and negative LLEs, respectively); while the other PPs are based on the number of isospikes for I_x ((b) and (e)), and I_y ((c) and (f)). The color code identifying the number of isospikes is shown at the bottom. Parameter planes were obtained using the values stated in Table I, but with the value of the spin-flip relaxation rate $\gamma_s = 100$ n^{-1}. In the panels of the second row, we chose five points to obtain the time series and attractors to indicate their dynamic behavior. Each panel displays 1024×1024 pixels.

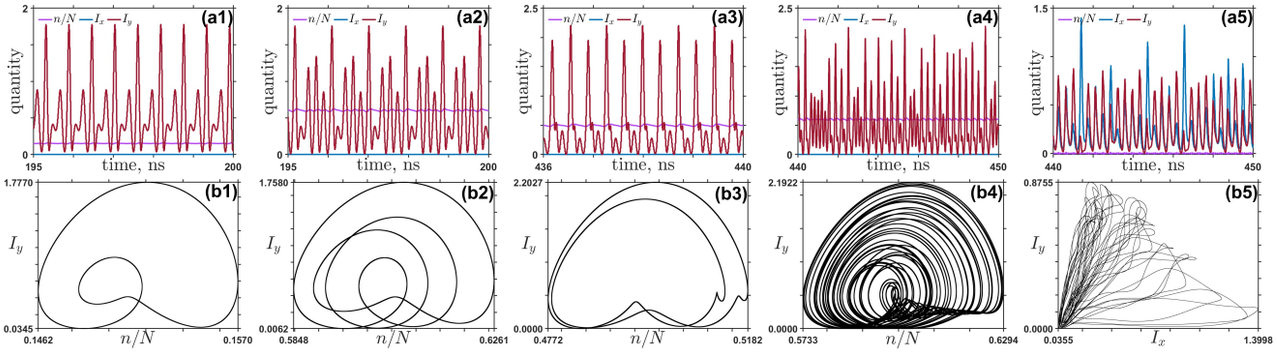

Figure 4. **First row:** Time series after a transient of 195 ns ((b1)–(b2)), 436 ns ((b3)–(b4)), and 440 ns (b5) for the dynamic quantities describing the VCSEL, i.e. n/N, I_x and I_y for the parameter values stated in Table I, but with $\gamma_s = 100 \times 10^9$ Hz with initial conditions $E_{xR}(0) = 0.2$, $E_{xI}(0) = 0.4$, $E_{yR}(0) = 0.3$, $E_{yI}(0) = 0.6$, $N(0) = 1.05$, and $n(0) = 0.05$ and $(\Delta\omega, E_{\rm inj})$ values for the PP points shown in Fig. 3(d) and (e): (a1) $(0.04, 40 \times 10^9)$, (a2) $(0.041, 44 \times 10^9)$, (a3) $(0.042, 73 \times 10^9)$, (a4) $(0.03, 57 \times 10^9)$, and (a5) $(0.01, 33 \times 10^9)$. **Second row:** Attractors corresponding to the panels above in the phase space section I_y vs. n/N, where limit cycles with (b1) three, (b2) five and (b3) six isospikes per complete oscillation are manifested and also (b4) a chaotic attractor in the quasicircular lobe region. (b5) Chaotic attractor in the phase space section I_y vs. I_x.

the dynamical behavior of VCSEL consists mainly of the use of the data coming from the numerical integration of Eqs. (2) for computing the Lyapunov spectrum with Wolf's method[76] from which we extract the largest Lyapunov exponent (LLE) and in some cases the second one for a better visualization of the transition regions in which the LLE is close to zero. Besides that, we proceed to the determination of the number of isospikes, that is, the number of maxima present during a cycle of a nonchaotic oscillation for some of the dynamical variables such as E_{xR}, E_{xI}, E_{yR}, and E_{yI}, or some quantities as I_x and I_y derived from the dynamical variables.

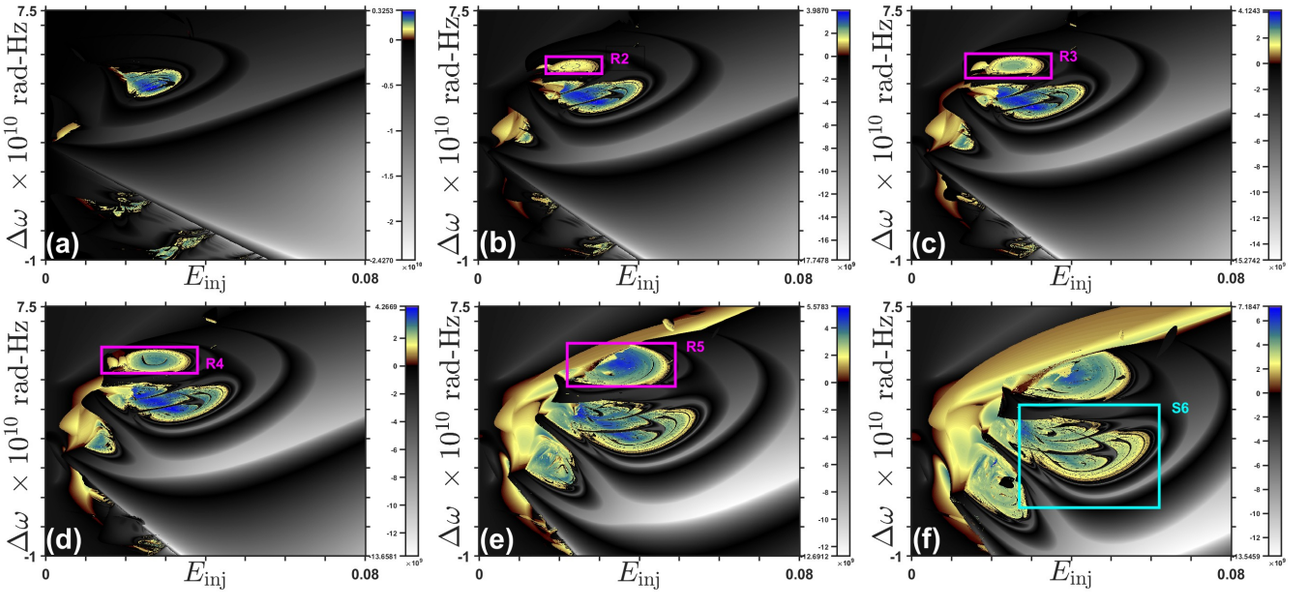

Figure 5. Parameter planes based on LLEs for different values of the linewidth enhancement factor (parameter α): (a) $\alpha = 1.50$, (b) $\alpha = 2.25$, (c) $\alpha = 2.50$, (d) $\alpha = 2.75$, (e) $\alpha = 3.75$, (f) $\alpha = 4.50$. Note that some regions were framed for further analysis. PPs were calculated using random initial conditions, a transient of 800 ns, and a total time of 1.6 µs; the time step being 1 ps. We note that in several parts of the PP, the regular regions are predominant and end with two branches giving rise to lobe structures where regular and chaotic regions are intermingled. Each panel displays 1024×1024 Lyapunov exponents.

III. RESULTS AND DISCUSSION

This section aims to present a comprehensive analysis of the VCSEL subjected to optical injection; to achieve this goal, we consider several aspects going from the notion of multistability to chirality and quint points. To characterize the VCSEL dynamical behavior, we explore the PP by computing the LLEs and the number of isospikes, which were complemented with time series, attractors, and indirectly by bifurcation diagrams. We start our analysis by choosing five dyads of the parameters $(E_{\rm inj}, \Delta\omega)$ to characterize the form of the time series and the shape of the corresponding attractors into a projection of the phase space shown in Fig. 1.

The first row panels of Fig. 1 show the time series features corresponding to the dynamical variables n/N, I_x, and I_y. In particular, we can observe in panel (a1) of Fig. 1 that all the considered quantities converge to a fixed point solution; on the other hand, from Fig. 1(b1) we can conclude that n/N attains a value close to zero very quickly, but at around 25.2 ns suddenly a chaotic oscillation (not shown but verified) takes place until around 82.3 ns, after which n/N reaches a stationary equilibrium, $n/N \approx 0.515$. A similar situation occurs for I_x. In contrast, I_y converges to equilibrium by damping oscillations. Figures 1(a2)–(a4) exhibit the time series in the presence of one, two, and four isospikes per oscillatory cycle, while Fig. 1(a5) shows chaotic oscillations. The second-row panels Figs. 1(b2)–(b5) display the section of the attractor in the plane I_y vs. n/N, one can thus appreciate how the different behaviors with one, two, and four isospikes translate into closed orbits with one loop, two loops, or four loops, respectively. The chaotic behavior of panel (a5) determines an intricate pattern shown in panel (b5).

1. *Multistability and polarization switching*

Due to the form of the nonlinear system describing a VCSEL subject to optical injection and also to previous works[34,54,70], it is expected intuitively the potential existence of multistability in the system. We start by showing in Fig. 2 the PPs ($\Delta\omega$ vs $E_{\rm inj}$) obtained by continuation using LLEs (global measurement) and isospikes for the intensities I_x and I_y; the continuation is done by tuning the value of $E_{\rm inj}$ by increasingly (first row) and by decreasingly (second row), while in the third row, we have a situation with fixed initial conditions at each time the $E_{\rm inj}$) value is changed but not for the changes in $\Delta\omega$; thus the continuation process is only in the $\Delta\omega$ parameter because when this parameter changes, the initial conditions are taken from the previous integration. As can be seen in the PPs of each column, they are similar but with notable differences; for instance, when comparing the PPs of the first column, we observe that the attained values (represented by using a color scheme) are slightly different, indicating some global unlikeliness in the dynamic behavior. Moreover, when the continuation process is performed by decreasing the value of $E_{\rm inj}$), we note that for small values of $E_{\rm inj}$), there is a chaotic behavior (Fig. 2(d)), a situation that is not observed for the other cases Figs. 2(a) and (g). Concerning the second column that shows PPs for the intensity I_x, we found a different behavior for the continuation process again by decreasing the value of $E_{\rm inj}$), where most of the PP shown

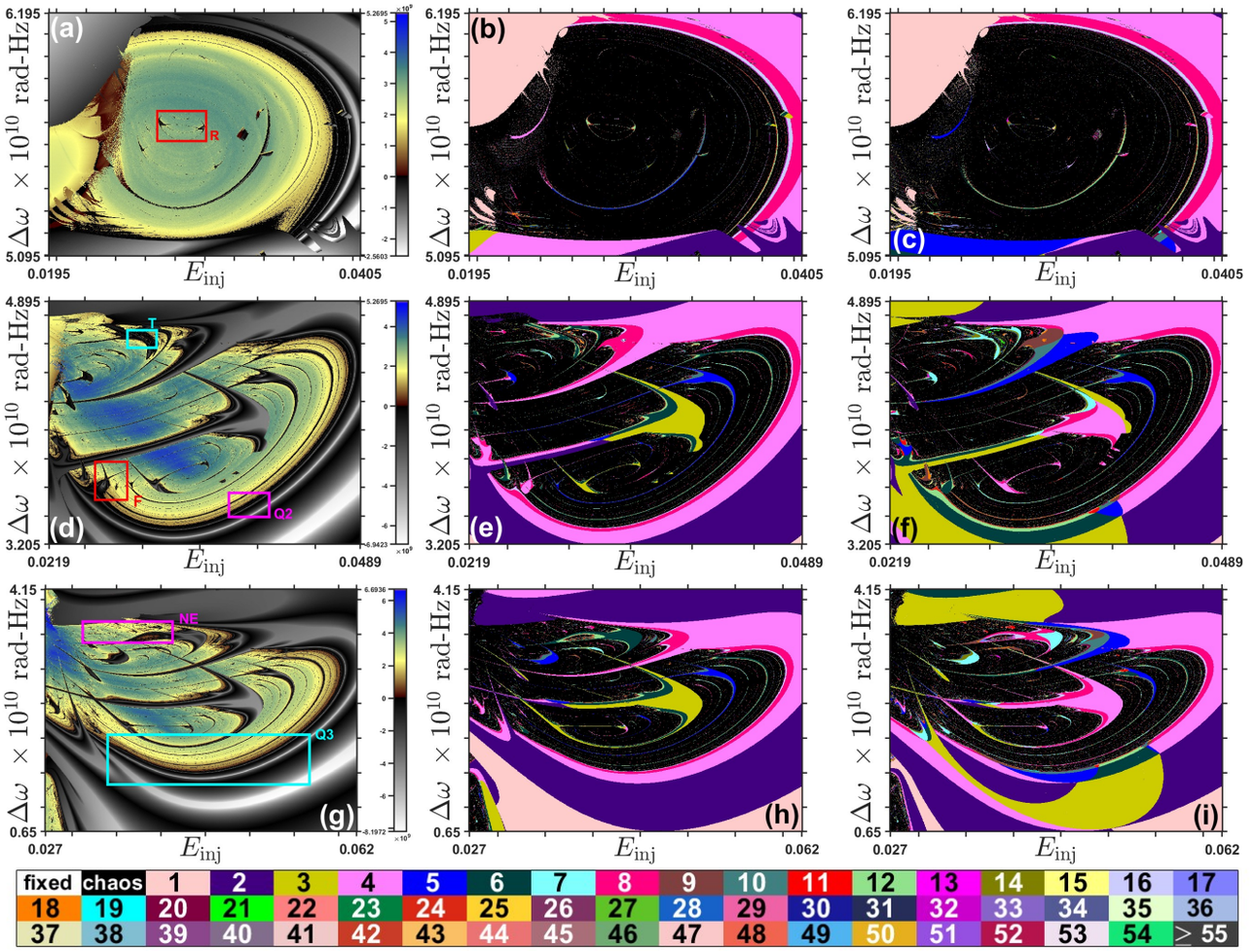

Figure 6. Lobe structures in the plane $\Delta\omega$ vs $E_{\rm inj}$ of the Fig. 2(g)'s framed regions A and B. These PPs are based on LLEs (global measure) shown in the first column and the number of isospikes in the second and third columns; panels (b) and (e) represent the PPs that describe the dynamics of I_y, while (c) and (f) those of the component E_{yI}. The linewidth enhancement factor is $\alpha = 3.0$ for the first and second rows and $\alpha = 4.5$ for the third row. At the bottom, the color code identifies the dynamic behavior: fixed point, chaos, or the number of isospikes or maxima per oscillation of (b)–(c) and (e)–(f). Each panel has a resolution of 1024×1024 pixels.

in Fig. 2(e) exhibits a fixed-point behavior with some tiny regions of chaotic or oscillatory behavior with one isospike per oscillation. On the contrary, the PPs shown in Figs. 2(b) and (h) depict the boundaries of the polarization switching (PS), which is the most dramatic revelation of the polarization instabilities[1]. Indeed, thanks to the isospikes-based PP of I_x, it is possible to determine the phenomenon of PS off (x-LP mode off) and PS on (x-LP mode on) when varying the optical injection as shown in Figs. 2(b) and (h). The last column shows the isospikes-based PPs for I_y related to the y-LP mode, where the rich dynamical behavior of this quantity is featured with the number of isospikes per oscillation indicated in the color code and fixed-point and chaotic behavior represented by white and black respectively. Note the presence in Figs. 2(a)–(b) of specific points identified with a number; for these points on the PP, we represent in Fig. 1 the time series for the variables n/N, I_x and I_y (first row) and the attractors in terms of I_y vs n/N (second row). In Fig. 2(c) are identified the dynamic behaviors of each of the five considered points in Figs. 2(a)–(b)., according to the color code shown at the bottom.

The inspection of the panels shown in Fig. 2 indicates the multistability of the system due to the changes in the PPs' landscapes as a result of the variations in the initial conditions. The presence of chaotic regions on the PPs intermingled with structures indicating regular behavior is the signature of the rich dynamical behavior of the system. Therefore, the differences exhibited in the panels of the second row in Fig. 2 are not surprising even though they may initially suggest numerical inconsistencies. We selected in Fig. 2(g) two rectangular regions with these characteristics (A and B) that will be used for further analysis in Sect. III 2.

The results presented in Fig. 3 have been obtained by changing the parameter associated with the spin-flip relaxation rate and setting it to $\gamma_s = 100$ ns^{-1}. We consider two cases, the first in which the initial conditions are randomly se-

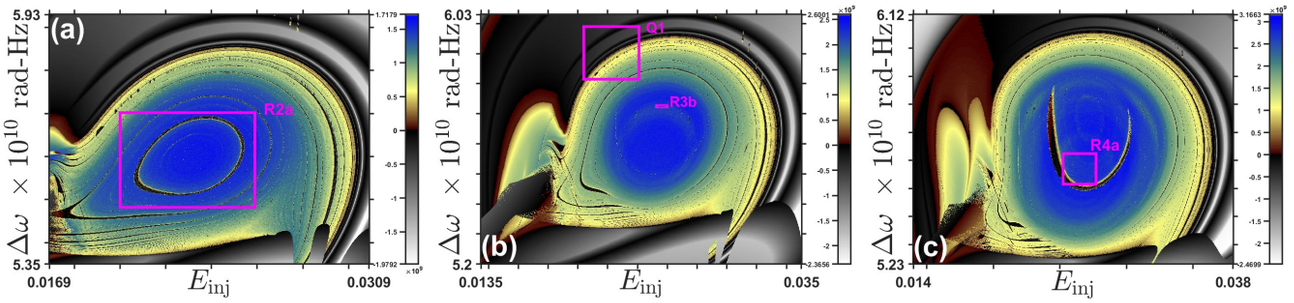

Figure 7. Parameter planes based on LLEs for the lobe structures wherein ring structures are immersed when the linewidth enhancement factor (parameter α) are: (a) $\alpha = 2.25$, (b) $\alpha = 2.50$, and (c) $\alpha = 2.75$. The panels come from the framed regions R2–4 in Fig. 6(b)–(d) respectively.

lected and updated at the end of each integration of a point on the PP (first row) and the second for which the initial conditions are fixed to those indicated in Fig. 2 and by starting each integration with the same initial conditions (second row). We observe that all the PPs are similar but small differences are visible; for example, when comparing the PPs based on LLE, the only difference is that the maximum LLE ($\lambda_{\max}$) overall PP in Fig. 3(a) is $\lambda_{\max} = 4.7059 \times 10^9$ Hz and for Fig. 3(d) is $\lambda_{\max} = 4.6743 \times 10^9$, this little difference in the LLEs related to chaotic behavior could be explained by the fact that with random initial conditions, some of them could be related to longer transients. Consequently, from a statistical point of view, such situations tend to increase the maximum LLE slightly. When comparing PPs related to I_x, we observe more differences between PPs, that is, the variables related to x-LP mode are more sensitive to changes in initial conditions as has been observed in the second column of PPs in Fig. 2, although their dynamics are not as richer as in the case of variables related to y-LP mode.

In Fig. 4 we report the time series associated with the parameter values corresponding to the points marked on the panels of the second row of Fig. 3. These choices have been made according to the dynamic behavior of interest exhibited in Fig. 3(e)–(f). The expected behavior of the specific situation is corroborated by Fig. 4. In particular, it is interesting to note that points 4 and 5 related to chaotic behavior have remarkable differences, although both exhibit chaotic behavior.

2. *Lobe regions*

An interesting issue pointed out in Sect. III 1 is the identification of lobe regions where the dynamic behavior looks richer due to chaotic behavior and the presence of interesting structures inside the PP, which allows us to study their dynamic features.

Figure 5 shows the PPs $\Delta\omega$ vs $E_{\rm inj}$ for several values of the linewidth enhancement factor (α), wherein each panel exhibits several regular and chaotic regions characterized by the fact of being immersed into lobe regions. From a global viewpoint, regular regions are predominant and, in general, they end with two branches, giving rise to lobe structures where regular and chaotic regions are intermingled. We also observe that the abundance of chaotic regions increases with α. We can identify two types of lobe regions, one having a circular shape that contains some ring structures as those described in[60] in the framework of modeling the dynamics of cancerous cell population[61], a VCSEL and the Hartley circuit[60]. We emphasize those structures by drawing a box around them, and we name the latter by R2, R3, R4 and R5 in Figs. 5(b)–(e); Sect. III 3 will be devoted to their study. On the other hand, there are other lobe structures denoted by S6 in Fig. 5(f) which contain interesting structures going from spirals to multishrimps; the latter will be studied in Sects. III 4 and III 5. Each panel displays the Lyapunov exponent computed on a mesh of 1024×1024 random initial conditions, with a total integration time of 1.6 μs, a transient of 800 ns and a time step of 1 ps.

Figure 6 shows in its first column the boxes A (panel (a)) and B (panel (d)) of Fig 2(g), and the box S6 (panel (g)) of Fig. 5(f) in terms of LLEs. The dynamics of the I_y variable (middle column) and the component E_{yI} (right column) are characterized using isospikes. Note that PPs based on LLE exhibit similar values, that is, similar color scale, to the ones of Fig. 2(g). It should be noted that there is a similarity between panels based on LLE (global measure) and those based on isospikes for the observable I_y and the dynamic variable E_{yI}. On the other hand, the diagrams based on isospikes give more details about the dynamics, where, for instance, in the panels of the first row, we can see some bishrimp structures, in such a way that they are joined by their "legs" and "antennae". Although diagrams (b) and (c) are very similar at first sight, we would like to notice that the joined shrimps in panel (b) have the same number of isospikes, whereas in panel (c) the constituting shrimps have different numbers of isospikes. These ring structures and other features are explained in more detail in Sect. III 3.

To summarize the lobe structures, we point out that in the observed LLE-based PPs in Figs. 2, 3, and 5, there are huge regular regions in lobe form ending by two branches giving rise to other regular regions in the form of shrimps and fishes immersed in chaotic regions. We selected various boxes that are zoomed in Figs. 6(a), (d), and (g), each of which focuses on different features. In Fig. 6(a) there are two lobe regions in which chaotic and regular behavior appear; the regularity is manifested by rounded bishrimp-like structures (red box

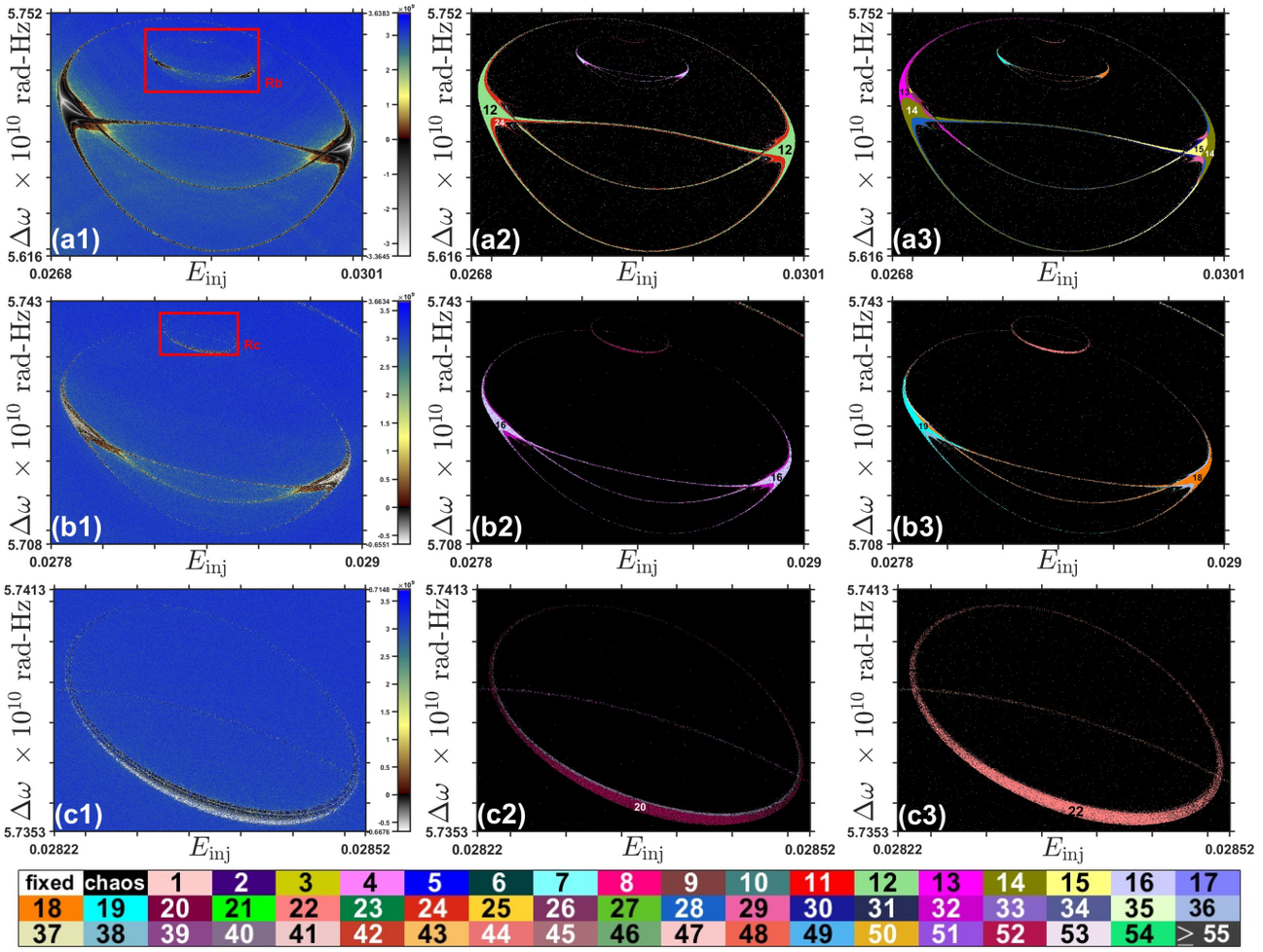

Figure 8. (a1) Sequence of ring structures in the plane $\Delta\omega$ vs $E_{\rm inj}$ of the framed region in Fig. 6(a). Magnification of frames (b1) Rb and (c1) Rc. The sequence represents a kind of "shrimp annihilation" process where the succession of bishrimp ring structures ends in a ring structure with no vestige of shrimps. Parameter planes based on LLEs (global measure) are depicted in the left column (a1,b1 and c1). Panels in the central and right column represent the PPs describing the dynamics for I_y (a2,b2 and c2) and E_{yI} (a3,b3 and c3) respectively, and in terms of the number of isospikes. At the bottom, the color code identifies the dynamic behavior: fixed point, chaos, or the number of isospikes per oscillation of the isospikes-based diagrams of the central and right columns panels. Each panel has a resolution of 1024×1024 pixels.

R whose magnified sequence is shown in Fig. 8(a1)-(b1)), a fish-like structure is shown in box F of Fig. 6(d) whose main feature compared to the shrimp-like structure lies in the fact that there are no antennae. Shrimp-like structures, and fish-like structures (cyan box) that are magnified in Fig. 6(g). The regular ones generate "primordial" shrimp or fish structures surrounded by chaotic regions and also allow one to observe spiral structures that appear more clearly with increasing values of α (compare the diagrams of the second ($\alpha = 3.0$) and third ($\alpha = 4.5$) rows of Fig. 6.

3. *Ring structures*

Ring structures appear in PPs in different kinds of systems as stated in Sect. I. Looking at Figs. 6(a)–(c) we can observe the presence of ring structures generated by bishrimps that end by a ring structure resembling a shrimp-annihilation process as shown in Fig. 8. On the other hand, the lobe regions framed in Fig. 5(b)–(d) are shown in Fig. 7. We observe in all three cases the presence of ring structures whose dependence on LLEs, the number of isospikes for the quantities I_y and E_{yI}, is emphasized in Fig. 9 by showing a magnified view. From the same Fig. 9 we can again observe the ring structures inside the lobe structures.

The parameter range associated with box R in Fig.6(a) is shown on a larger scale in Fig.8(a1), where the sequence of bishrimp structures is clearer; observe also that another bishrimp structure appears (marked by the box Rb and shown in Fig.8(b1)). In Fig.8(c1), no trace of the bishrimp structure remains. Only a ring structure is visible as a result of "shrimp annihilation." The finest details for the variable I_y are shown in the central column panels, where the main periodicities for the bishrimps are 12 isospikes (panel (a2)) and

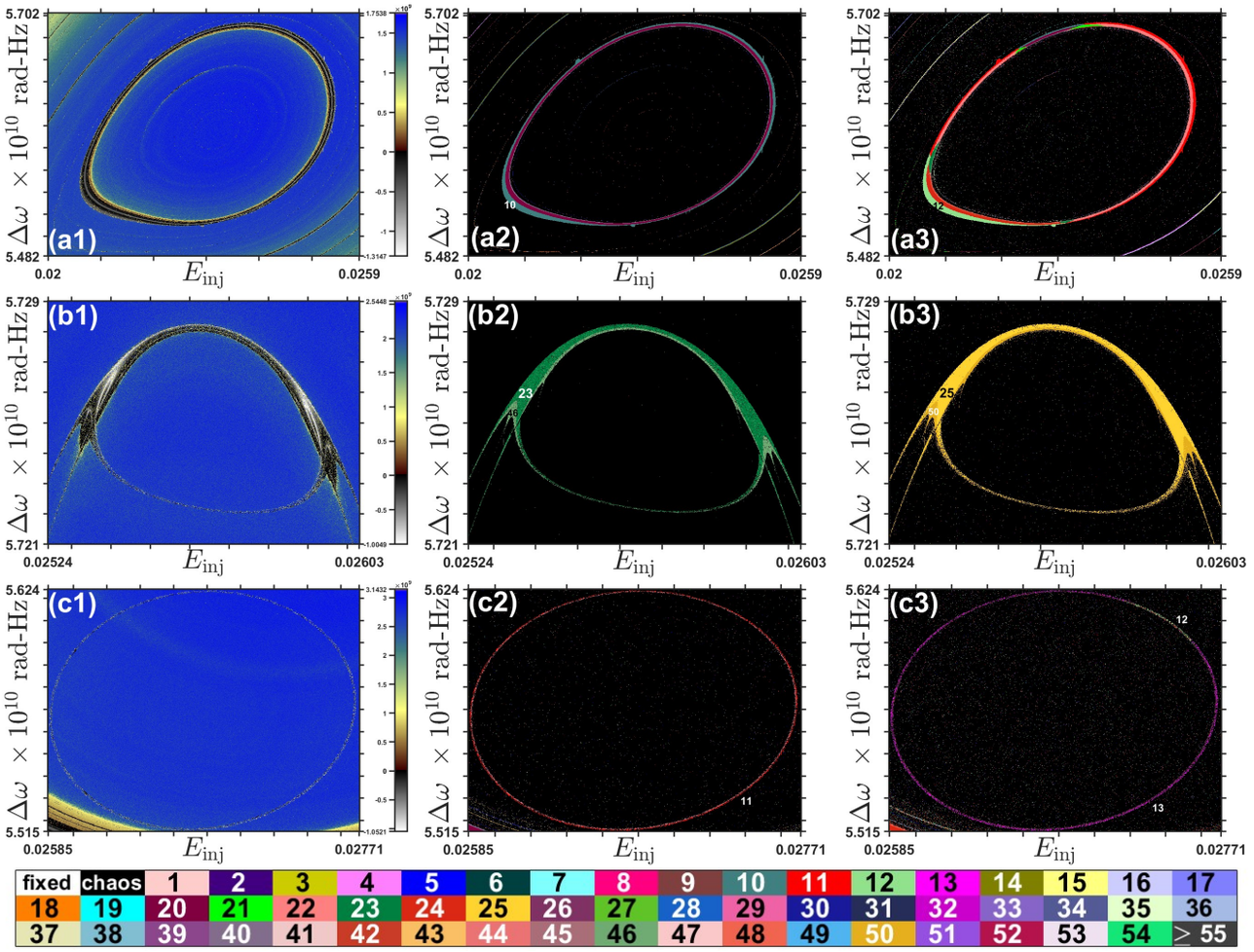

Figure 9. Ring structures in the plane $\Delta\omega$ vs $E_{\rm inj}$ of the framed region in Figs. 7(a)–(c). The PPs based on LLEs (global measure) are depicted in the left column (a1, b1 and c1). The panels in the central and right columns represent the PPs that describe the dynamics for I_y (a2, b2 and c2) and E_{yI} (a3, b3 and c3) respectively, and in terms of the number of isospikes. The values of the linewidth enhancement factor for the panels of the first, second and third rows are $\alpha = 2.25$ (a1-a3), $\alpha = 2.50$ (b1-b3) and $\alpha = 2.75$ (c1-c3) respectively. At the bottom, the color code identifies the dynamic behavior: fixed point, chaos, or the number of isospikes per oscillation of the second and third columns. Each panel has a resolution of 1024×1024 pixels.

16 isospikes (panel (b2)). In comparison, the ring structure (panel (c2)) exhibits 20 isospikes. It is noteworthy the presence of period-doubling bifurcations (isospikes duplication) in the route to chaos. The diagrams for the component E_{yI} located in the right column are more intricate because in (a3), the shrimp exhibit two main periodicities: 14 and 15 isospikes for the right-located shrimp and 13 and 14 for the left-located one. As a consequence, the route to chaos is not a simple period-doubling cascade. In (b3), the difference in the periodicities is still present with 18 and 19 isospikes for the shrimps located right and left, respectively. Finally, the resulting ring structure shown in (c3) has a main periodicity of 22 isospikes and the route to chaos is simply described by a period-doubling cascade. Now, considering the lobe structures found in Fig. 5, and selecting the boxes R2, R3 and R4 of panels (b)–(d) which are zoomed in Fig. 7, we observe again the emergence of ring structures of different nature as detailed by zooming the boxes R2a, R3b and R4a of panels (a)–(c) in the panels of the first column of Fig. 9, where the ring structures can be distinguished as describing regular behavior (see the color bar accompanying every LLE-based PP). We complement the analysis using isospikes diagrams for the variable I_y (central column) and the component E_{yI} (right column). We observe in the sequences going from first to third rows, the different nature of the ring structures. In the first row, there is a well-defined ring with a periodicity of 10 isospikes for I_y and with a period-doubling (duplication of the number of isospikes) in the route to chaos towards the concave part; on the other hand, for E_{yI}, there are two dominant periodicities of 11 and 12 isospikes with the consequence that it is not a period-doubling route to chaos as usually observed. In the second row, we see that the ring structure is formed by the coalescence of one antenna and one leg with a main periodicity of 23 and 25 for I_y and E_{yI} respectively; in both cases, period-

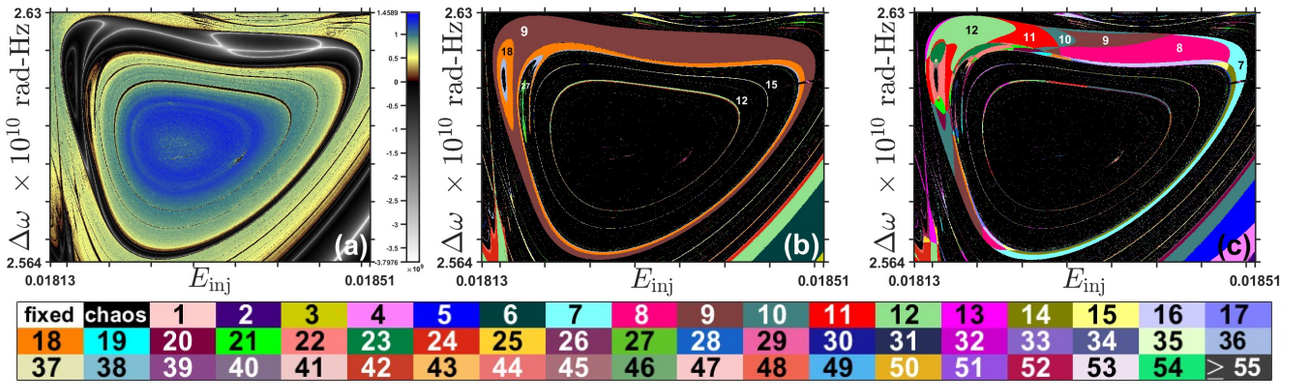

Figure 10. Ring structures in the plane $\Delta\omega$ vs $E_{\rm inj}$ of the framed region in Fig. 6(d). The parameter values are those stated in Table I. Dynamical behavior is described in terms of (a) Largest Lyapunov exponents (global measure) and isospikes for quantities (b) I_y and (c) E_{yI}. At the bottom, the color code identifies the dynamic behavior.

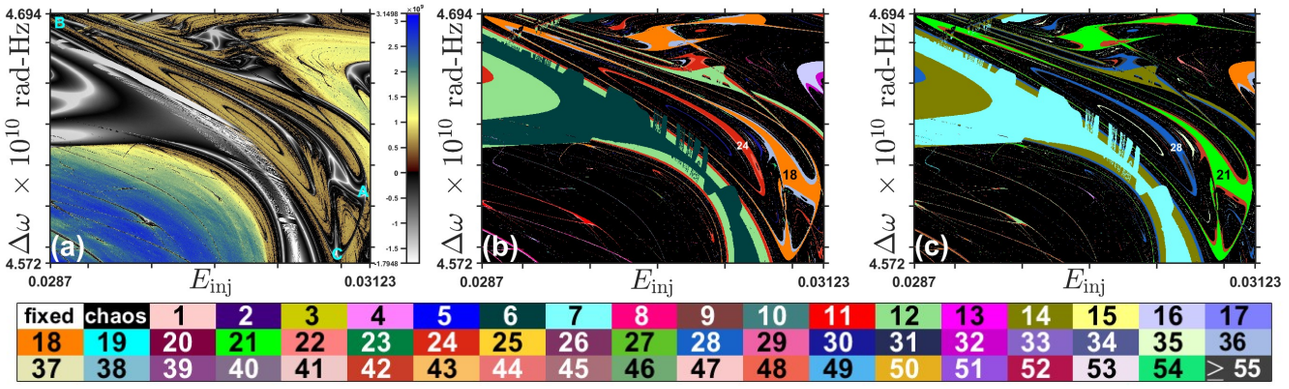

Figure 11. Tricorn-like structure in the plane $\Delta\omega$ vs $E_{\rm inj}$ of the framed region in Fig. 6(d). The parameter values are those stated in Table I. Dynamical behavior is described in terms of (a) LLEs (global measure) and isospikes for quantities (b) I_y and (c) E_{yI}. At the bottom, the color code identifies the dynamic behavior.

doubling is manifested. Finally, in the third row, there is a fine and almost circular ring structure with the main periodicity of 11 isospikes for I_y and 12 and 13 isospikes for E_{yI}; thus it is not a period-doubling route to chaos as commonly observed.

To conclude our analysis of the ring structures, we consider the lobe region framed in the red box C shown in Fig. 2(g). From this region, we chose the part that contains a ring structure as illustrated in Fig. 10 in terms of LLE (panel (a)) and isospikes (panel (b) for I_y and panel (c) for E_{yI}). The shapes of the regions indicating regular dynamical behavior (ring structures) are quite similar. We observe in the three panels the presence of several other ring structures inside the main one. Figure 10(a) indicates that the central part exhibits a higher LLE with the possibility of finding hyperchaotic behavior when going further in the study of the Lyapunov spectrum; on the contrary, the white lines appearing on the top of the main ring structure might reveal the existence of superstable orbits. Roughly speaking, we associate the superstable tracks to the curves exhibiting the lower LEs inside a shrimp or other structure denoting regular dynamic behavior; the intersection of these tracks may constitute the locus of superstable orbits. The analysis of Fig. 10(b) allows us to identify some interesting aspects such as the presence, on the upper left of the ring, of the so-called "eye of chaos" as has been observed in forced systems such as a Brusselator[25] and an autocatalator[59]. In Fig. 10(c), the ring structure for E_{yI} contains several main periodicities going from 7 to 12 isospikes with intricate distribution and even exhibiting quint points in opposition to that of I_y whose main periodicity is 9 isospikes and showing a distribution corresponding to a period-doubling.

4. *Other multishrimp structures*

In Sect. III 3 we focus on ring structures that generally emerge from two shrimps merging in a closed structure either by joining their legs, antennae, or both.

In addition to the bishrimp structures, we also found closed structures formed by three shrimps as tricorn-shaped structures such as those observed in a model of a semiconductor laser[15] and those analyzed in detail in a quartic map[45]. Figure 11 coming from the box T of Fig. 6(d) illustrates such structures in the PP $\Delta\omega$ vs $E_{\rm inj}$ where it is possible to identify the coalescence of three shrimps that join their "heads"

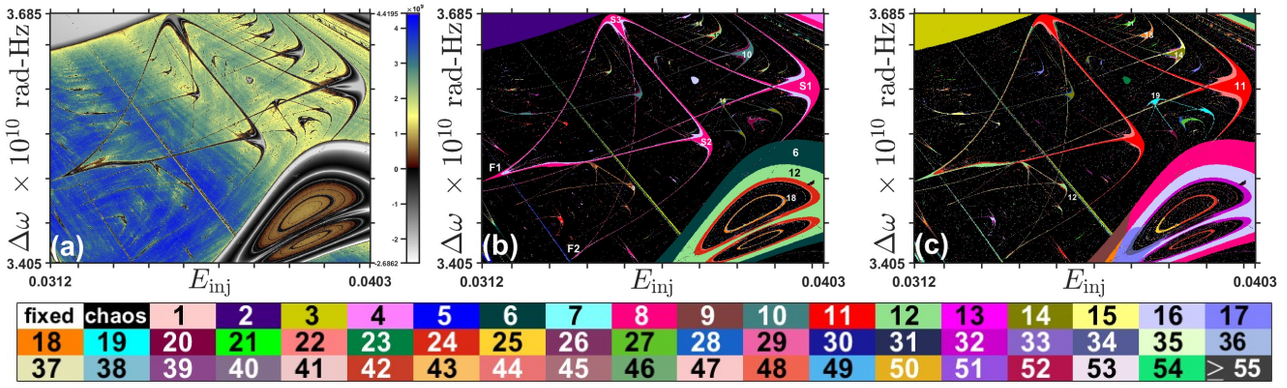

Figure 12. Shrimp network structure in the plane $\Delta\omega$ vs $E_{\rm inj}$ of the framed region in Fig. 6(d). The parameter values are those stated in Table I. Dynamical behavior is described in terms of (a) LLEs (global measure) and isospikes for quantities (b) I_y and (c) E_{yI}. At the bottom, the color code identifies the dynamic behavior.

by their "antennae" and the individual legs of a shrimp fuse as it happens in mermaids; finally, under these conditions, the fused legs of all shrimps join those of the other shrimps, resulting in the formation of three closed parts of the tricorn-like structure. On the other hand, ring structures appear inside the closed parts mentioned above. In Fig. 11(a) we denote shrimp's heads with A, B, and C. and we note the existence of superstable tracks represented by white lines, wherein the intersection of the shrimp-fused legs the abundance of such superstable tracks is more prominent. The tricorn-like structures shown in Figs. 11(b)–(c) correspond to the PPs of I_y and E_{yI} respectively and only differ by the fact that the main periodicities in each case are 18 and 21 isospikes and the ring structures contained inside the chaotic predominant regions have 24, 30, ... for I_y, and 27, 35, ... for E_{Iy}; in both cases, there is a period-doubling bifurcation.

Finally, by considering the box NE of Fig. 6(g), we represent the framed region in Fig. 12, where in panel (a) the LLE-based PP reveals the presence of a network composed of three shrimps and two fishes, we also note a shrimp sequence going towards a superstable region characterized by small values of the LLEs; it is possible to identify in the lower-right part of the panel a structure exhibiting the so-called "eyes of chaos" shown when analyzing Chua's circuit[48] and reported recently in[62] in a discrete neuron model, where inside the "eyes orbits" there are several ring structures. In Fig. 12(b), and working with the number of isospikes for the dynamical representation of I_y, we focus on the network with the identification of shrimp and fish denoted by S1, S2, S3 F1 and F2, whose "heads" constitute the nodes of a network and the antennae and legs serve to establish the connections. As the main periodicity of all nodes and links is the same (8 isospikes), we assume the simplest representation of the network, i.e., an undirected and unweighted adjacency matrix shown in Eq. (3)

$$A = \begin{pmatrix} 0 & 0 & 1 & 0 & 0 \\ 0 & 0 & 1 & 1 & 1 \\ 1 & 1 & 0 & 1 & 1 \\ 0 & 1 & 1 & 0 & 0 \\ 0 & 1 & 1 & 0 & 0 \end{pmatrix}, \tag{3}$$

where the columns (rows) correspond to nodes S1, S2, S3, F1, F2. It is interesting to note that other similar but smaller networks with periodicities 9 and 14 appear beside the network characterized by A. A similar scenario is depicted for the diagram of panel (c) corresponding to the E_{yI}; nevertheless, in this case, the fish-like structures have a different main periodicity (12 isospikes) than the shrimp-like structures (11 isospikes) suggesting that the network representation might be modified considering the directional feature of the connections; we believe that such analysis is beyond the scope of this work, but undoubtedly this kind of ideas remain worth studying for further analysis and even it would be interesting to express the different bishrimp and multishrimp structures in terms of a network representation. Concerning smaller networks, they have as main periodicity 12 and 19 isospikes. The shrimp sequences of I_y and E_{yI} go to structures of 2 and 3 isospikes, respectively, and the shrimp-periodicity increases as 8 - 10 - 12 - 14 -..., and 11 - 14 - 18 - 21 -.... Note the discrepancy in the sequence between 14 and 18 (4 isospikes of difference instead of 3). Finally, the structures containing the "eyes of chaos" exhibit a main periodicity of 6 isospikes and present a period-doubling sequence; moreover, the ring structure inside the eyes orbits is 18 isospikes for I_y. In contrast, there are several periodicities of the structure for E_{yI} and the isospikes distribution is much more intricate. Note the presence of quint points in the structure that will be discussed in more detail in Sect. III 5.

5. *Chirality and quint points*

The concept of quint points is related to a specific set of conditions in which distinct phases coexist in physical phase diagrams[4]. In the present cases, there are triple, quart, and quint points corresponding to three, four, and five coexisting phases; notably, the quint points are concerned with some chiral properties in the phase diagrams. In the last three years, several works have dealt with these peculiar points, chemical reactions[17,23,25,26], electronic circuits[22,73], mechanical sys-

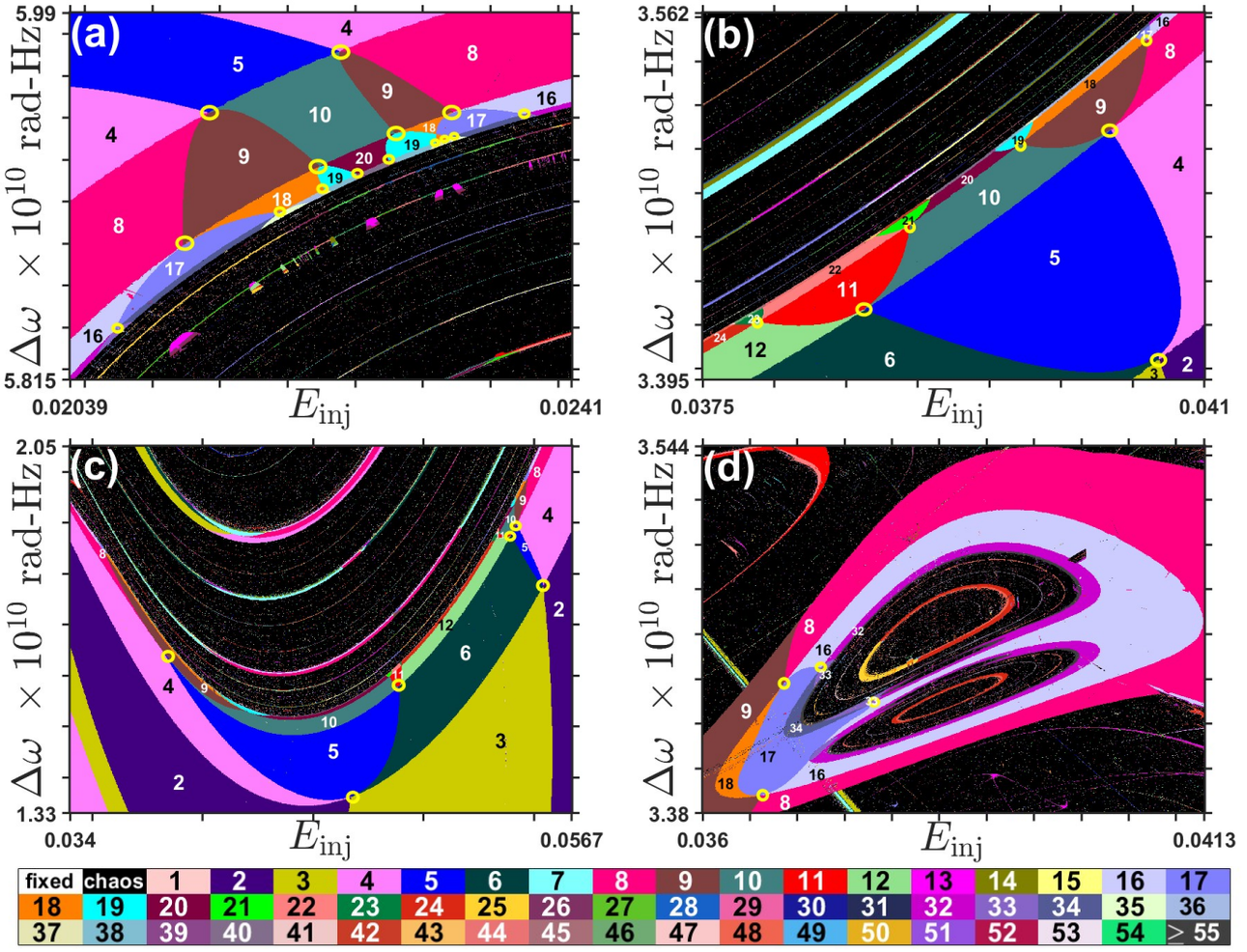

Figure 13. Quint points structure in the plane $\Delta\omega$ vs $E_{\rm inj}$ of the boxes (a) Q1 from Fig. 7(b), (b) Q2 from Fig. 6(d), (c) Q3 from Fig. 6(g), and (d) the "eyes of chaos" structures of Fig. 12(c). The description is based on the number of isospikes and considering the component E_{yI}. At the bottom, the color code identifies the dynamic behavior.

tems[41,44,77], and also in a free-running VCSEL[30], to mention a few. We perform our analysis considering, in all cases, the dynamical description of the component E_{yI} in terms of the number of isospikes. The box Q1 from Fig. 7(b) is represented in Fig. 13(a); we observe the route to chaos via a sequence of Feigenbaum cascade in which there are several quint points marked with a circle, each of one indicating the coexistence of five phases.

Figure 14 shows a simplified view of the occurrence of the chaos route through unfolding chiral structures in the downward and upward concavity corresponding to those appearing in the PPs shown in Figs. 13(a) and (c). Note that the chiral unfoldings that we found occur in all cases associated with concavities, but not necessarily in closed structures such as those studied in[23,25]; nevertheless, Fig. 13(d) exhibits the structure mentioned above. We also point out in the schema shown in Figs. 14(a)–(b) the sequence of periodicities in terms of isospikes considering the four main layers and its generalization to n layers, A last remark is related to Fig. 13(c), which shows a kind of bifurcation diagram inside the PP reminding us of a typical Feigenbaum cascade.

IV. CONCLUDING REMARKS

In this work, we performed an in-depth analysis of the VCSEL by using mainly the largest Lyapunov exponents and the number of isospikes to analyze the parameter plane; this allowed us to show the importance of our method of identification of polarization switching in the VCSEL and also the possibility of controlling the dynamics of the system. We provide strong support for the multistable nature of the system. On the other hand, we identify lobe regions that are the parts of the parameter planes where the system's dynamical richness is strengthened; in particular, we studied the role of the linewidth enhancement factor (i.e., the parameter α) on the apparition of different dynamical structures. Our analysis revealed several interesting structures in the parameter plane, for instance,

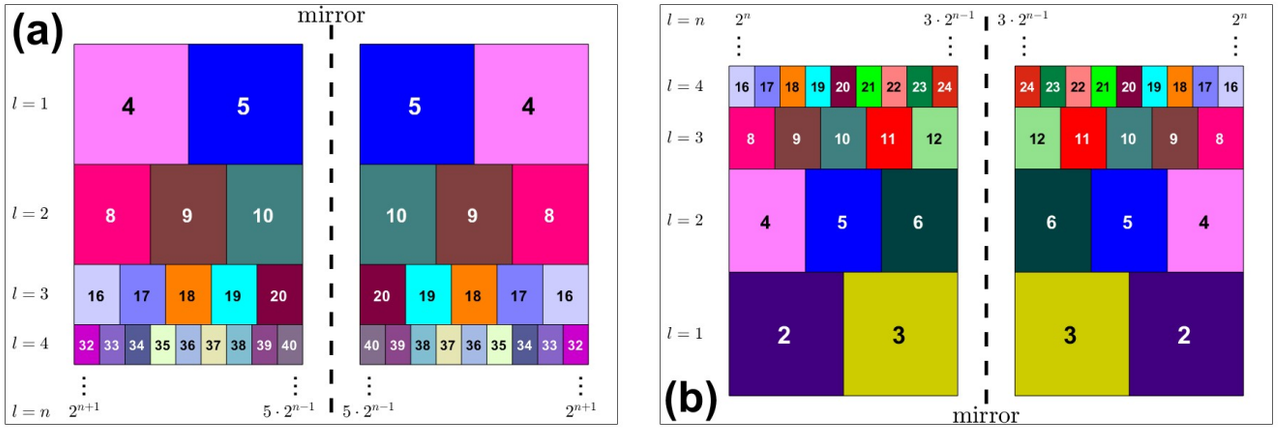

Figure 14. Simplified representation of the route to chaos via chiral unfolding observed in the precedent figure. (a) Concavity downward and basis periodicity 5 (Fig. 13(a)). (b) Concavity upward and basis periodicity 3.

those composed of two or more shrimps, and a diversity of ring structures resulting from a two-shrimps annihilation-like process. We also found some tricorn-shaped structures resulting from the fusion of shrimp in which their "legs" fuse together as in sirenomelia pathology (mermaid syndrome). We also studied the structure of the rings within the three closed regions resulting from the shrimp fusion. Perhaps, our most important finding is the introduction of the network structure capable of relating three shrimp-like and two fish-like structures. The detection of the abundant presence of quint points and chirality is another important result of this work. Additionally, we also detected the eye(s) of chaos structures. The importance of our approach lies in the fact that, for this kind of system, it is crucial to have a global measure of the system's dynamics (e.g., given by the Lyapunov exponents) and also to extract the finest dynamics details for each one of the relevant dynamical variables through the determination of the number of isospikes (local measure). This characteristic of our approach has been essential to unraveling the practical involvements of the system, but also to finding novel dynamic features such as the multishrimp networks. We hope that this kind of analysis might motivate the experimental scientists to corroborate the above-mentioned findings.

ACKNOWLEDGMENTS

GMRA acknowledges Jason Gallas for motivating the study of VCSELs, and this paper is dedicated to him for his invaluable contribution to nonlinear science. This project has received funding from the European Union's Horizon 2020 research and innovation programme under the Marie Sklodowska-Curie grant agreement No 101034383. Computational resources have been provided by the Consortium des Équipements de Calcul Intensif (CÉCI), funded by the Fonds de la Recherche Scientifique de Belgique (F.R.S.-FNRS) under Grant No. 2.5020.11 and by the Walloon Region.

AUTHOR DECLARATIONS

Conflict of Interest

The authors have no conflicts to disclose.

Author Contributions

G. M. Ramírez-Ávila: Conceptualization (equal); Formal analysis (equal); Investigation (equal); Methodology (equal); Software (lead); Validation (equal); Visualization (equal); Writing — review & editing (equal). **T. Carletti:** Conceptualization (equal); Formal analysis (equal); Investigation (equal); Methodology (equal); Validation (equal); Visualization (equal); Writing — review & editing (equal); Resources (lead).

DATA AVAILABILITY

The data that support the findings of this study are available from the corresponding author upon reasonable request.

REFERENCES

[1] Ackemann, T.and Sondermann, M., "Characteristics of polarization switching from the low to the high frequency mode in vertical-cavity surface-emitting lasers," Appl. Phys. Lett. **78**, 3574–3576 (2001).
[2] Augustin, L. M., Smalbrugge, E., Choquette, K. D., Karouta, F., Strijbos, R. C., Verschaffelt, G., Geluk, E. J., van de Roer, T. G., and Thienpont, H., "Controlled polarization switching in VCSELs by means of asymmetric current injection," IEEE Photonics Technol. Lett. **16**, 708–710 (2004).
[3] Barrio, R., "Sensitivity tools vs. Poincaré sections," Chaos Soliton. Fract. **25**, 711–726 (2005).
[4] Berlinsky, A. J.and Harris, A. B., *Statistical Mechanics: An Introductory Graduate Course* (Springer Nature, Cham, 2019).
[5] Bonatto, C., "Hyperchaotic dynamics for light polarization in a laser diode," Phys. Rev. Lett. **120**, 163902 (2018).

[6]Bonatto, C.and Endler, A., "Extreme and superextreme events in a loss-modulated CO_2 laser: Nonlinear resonance route and precursors," Phys. Rev. E **96**, 012216 (2017).
[7]Bonatto, C., Feyereisen, M., Barland, S., Giudici, M., Masoller, C., Leite, J. R. R., and Tredicce, J. R., "Deterministic optical Rogue waves," Phys. Rev. Lett. **107**, 053901 (2011).
[8]Bonatto, C.and Gallas, J. A. C., "Accumulation horizons and period adding in optically injected semiconductor lasers," Phys. Rev. E **75**, 055204–4 (2007).
[9]Bonatto, C.and Gallas, J. A. C., "Accumulation boundaries: codimension-two accumulation of accumulations in phase diagrams of semiconductor lasers, electric circuits, atmospheric and chemical oscillators," Phil. Trans. R. Soc. A **366**, 505–517 (2008), 10.1098/rsta.2007.2107.
[10]Bonatto, C.and Gallas, J. A. C., "Periodicity hub and nested spirals in the phase diagram of a simple resistive circuit," Phys. Rev. Lett. **101**, 054101–4 (2008).
[11]Bonatto, C., Garreau, J., and Gallas, J. A. C., "Self-similarities in the frequency-amplitude space of a loss-modulated CO_2 laser," Phys. Rev. Lett. **95**, 143905 (2005).
[12]Bosco, N. D., Rech, P. C., Beims, M. W., and Manchein, C., "Influence of sinusoidal forcing on the master fitzhugh–nagumo neuron model and global dynamics of a unidirectionally coupled two-neuron system," Chaos: An Interdisciplinary Journal of Nonlinear Science **34**, 093124 (2024).
[13]Burak, D., Moloney, J. V., and Binder, R., "Macroscopic versus microscopic description of polarization properties of optically anisotropic vertical-cavity surface-emitting lasers," IEEE J. Quantum Electron. **36**, 956–970 (2000).
[14]Chua, L., "Nonlinear circuits," IEEE Trans. Circuits Syst. I **31**, 69–87 (1984).
[15]Chávez, C. A. T.and Curilef, S., "Tricorn-like structures in an optically injected semiconductor laser," Chaos **30**, 023130 (2020).
[16]Jansen van Doorn, A. K., van Exter, M. P., van der Lee, A. M., and Woerdman, J. P., "Coupled-mode description for the polarization state of a vertical-cavity semiconductor laser," Phys. Rev. A **55**, 1473–1484 (1997).
[17]Field, R. J., Freire, J. G., and Gallas, J. A. C., "Quint points lattice in a driven Belousov–Zhabotinsky reaction model," Chaos **31**, 053124 (2021).
[18]Freire, J. G.and Gallas, J. A. C., "Stern–Brocot trees in cascades of mixed-mode oscillations and canards in the extended Bonhoeffer–van der Pol and the FitzHugh–Nagumo models of excitable systems," Phys. Lett. A **375**, 1097–1103 (2011).
[19]Gallas, J. A. C., "Structure of the parameter space of the Hénon map," Phys. Rev. Lett. **70**, 2714–2717 (1993).
[20]Gallas, J. A. C., "Dissecting shrimps: results for some one-dimensional physical models," Physica A **202**, 196–223 (1994).
[21]Gallas, J. A. C., "The structure of infinite periodic and chaotic hub cascades in phase diagrams of simple autonomous flows," Int. J. Bifurcat. Chaos **20**, 197–211 (2010).
[22]Gallas, J. A. C., "Chirality detected in Hartley's electronic oscillator," Eur. Phys. J. Plus **136**, 1048 (2021).
[23]Gallas, J. A. C., "Chirality observed in a driven ruthenium-catalyzed Belousov–Zhabotinsky reaction model," Phys. Chem. Chem. Phys. **23**, 25720–25726 (2021).
[24]Gallas, J. A. C., "Overlapping adding-doubling spikes cascades in a semiconductor laser proxy," Braz. J. Phys. **51**, 919–926 (2021).
[25]Gallas, J. A. C., "Non-quantum chirality in a driven Brusselator," J. Phys.: Condens. Matter **34**, 144002 (2022).
[26]Gallas, J. A. C.and Olsen, L. F., "Complexity in subnetworks of a peroxidase–oxidase reaction model," Chaos **32**, 063122 (2022).
[27]Gatare, I., Sciamanna, M., Buesa, J., Thienpont, H., and Panajotov, K., "Nonlinear dynamics accompanying polarization switching in vertical-cavity surface-emitting lasers with orthogonal optical injection," Appl. Phys. Lett. **88**, 101106 (2006).
[28]Gatare, I., Sciamanna, M., Nizette, M., and Panajotov, K., "Bifurcation to polarization switching and locking in vertical-cavity surface-emitting lasers with optical injection," Phys. Rev. A **76**, 031803 (2007).
[29]Gatare, I., Sciamanna, M., Nizette, M., Thienpont, H., and Panajotov, K., "Mapping of two-polarization-mode dynamics in vertical-cavity surface-emitting lasers with optical injection," Phys. Rev. E **80**, 026218 (2009).
[30]Gu, S., Zhou, P., and Li, N., "Non-quantum chiral structure in a free-running VCSEL," Opt. Lett. **48**, 2845–2848 (2023).
[31]Gu, S., Zhou, P., Mu, P., Guo, G., Liu, X., and Li, N., "Phase stability diagram, self-similar structures, and multistability in a free-running VCSEL with a small misalignment between the phase and amplitude anisotropies," Opt. Express **31**, 31853–31869 (2023).
[32]Hall, R. N., Fenner, G. E., Kingsley, J. D., Soltys, T. J., and Carlson, R. O., "Coherent light emission from GaAs junctions," Phys. Rev. Lett. **9**, 366–368 (1962).
[33]Hitzl, D. L.and Zele, F., "An exploration of the Hénon quadratic map," Physica D **14**, 305–326 (1985).
[34]Hurtado, A., Henning, I. D., and Adams, M. J., "Different forms of wavelength polarization switching and bistability in a 1.55 µm vertical-cavity surface-emitting laser under orthogonally polarized optical injection," Opt. Lett. **34**, 365–367 (2009).
[35]Hénon, M., "A two-dimensional mapping with a strange attractor," Commun. Math. Phys. **50**, 69–77 (1976).
[36]Iga, K., "Surface-emitting laser-its birth and generation of new optoelectronics field," IEEE J. Sel. Top. Quantum Electron. **6**, 1201–1215 (2000).
[37]Iga, K.and Li, H. E., *Vertical-Cavity Surface-Emitting Laser Devices* (Springer, Cham, 2003).
[38]Kovanis, V., Gavrielides, A., Simpson, T. B., and Liu, J. M., "Instabilities and chaos in optically injected semiconductor lasers," Appl. Phys. Lett. **67**, 2780–2782 (1995).
[39]Koyama, F., Kinoshita, S., and Iga, K., "Room-temperature continuous wave lasing characteristics of a GaAs vertical cavity surface-emitting laser," Appl. Phys. Lett. **55**, 221–222 (1989).
[40]Liu, Y., Takiguchi, Y., Davis, P., Aida, T., Saito, S., and Liu, J. M., "Experimental observation of complete chaos synchronization in semiconductor lasers," Appl. Phys. Lett. **80**, 4306–4308 (2002).
[41]Liu, Z., Rao, X., Gao, J., and Ding, S., "Non-quantum chirality and periodic islands in the driven double pendulum system," Chaos Soliton. Fract. **177**, 114254 (2023).
[42]Lorenz, E. N., "Deterministic nonperiodic flow," J. Atmos. Sci. **20**, 130–141 (1963).
[43]Lorenz, E. N., "Compound windows of the Hénon-map," Physica D **237**, 1689–1704 (2008).
[44]Manchein, C., Fusinato, B., Chagas, H. S., and Albuquerque, H. A., "Quint points lattice and multistability in a damped-driven curved carbon nanotube oscillator model," Chaos **33**, 063147 (2023).
[45]Maranhão, D. M.and Medrano-T, R. O., "Periodicity in the asymmetrical quartic map," Chaos Soliton. Fract. **186**, 115204 (2024).
[46]Martín-Regalado, J., Balle, S., and San Miguel, M., "Polarization and transverse-mode dynamics of gain-guided vertical-cavity surface-emitting lasers," Opt. Lett. **22**, 460–462 (1997).
[47]May, R. M., "Simple mathematical models with very complicated dynamics," Nature **261**, 459–467 (1976).
[48]Medrano-T, R. O.and Rocha, R., "The negative side of Chua's circuit parameter space: stability analysis, period-adding, basin of attraction metamorphoses, and experimental investigation," Int. J. Bifurcat. Chaos **24**, 1430025 (2014), doi: 10.1142/S0218127414300250.
[49]Mengue, A. D.and Essimbi, B. Z., "Symmetry chaotic attractors and bursting dynamics of semiconductor lasers subjected to optical injection," Chaos **22**, 013113 (2012).
[50]Michalzik, R., *VECSELs: Fundamentals, Technology and Applications of Vertical-Cavity Surface-Emitting Lasers* (Springer, Heidelberg, 2012).
[51]Milnor, J., "Remarks on iterated cubic maps," Exp. Math. **1**, 5–24 (1992).
[52]Ostermann, J. M.and Michalzik, R., "Polarization Control of VCSELs," in *VCSELs: Fundamentals, Technology and Applications of Vertical-Cavity Surface-Emitting Lasers*, edited by R. Michalzik (Springer, Berlin, 2013) pp. 147–179.
[53]Padullaparthi, B. D., Tatum, J., and Iga, K., *VCSEL Industry: Communication and Sensing* (John Wiley and Sons, Hoboken, New Jersey, 2022).
[54]Pan, Z. G., Jiang, S., Dagenais, M., Morgan, R. A., Kojima, K., Asom, M. T., Leibenguth, R. E., Guth, G. D., and Focht, M. W., "Optical injection induced polarization bistability in vertical-cavity surface-emitting lasers," Appl. Phys. Lett. **63**, 2999–3001 (1993).
[55]Panajotov, K.and Prati, F., "Polarization Dynamics of VCSELs," in *VCSELs: Fundamentals, Technology and Applications of Vertical-Cavity Surface-Emitting Lasers*, edited by R. Michalzik (Springer, Berlin, 2013) pp. 181–231.

[56]Quirce, A., Valle, A., Pesquera, L., Thienpont, H., and Panajotov, K., "Measurement of Temperature-Dependent Polarization Parameters in Long-Wavelength VCSELs," IEEE J. Sel. Top. Quantum Electron. **21**, 636–642 (2015).
[57]Raddo, T. R., Panajotov, K., Borges, B. H. V., and Virte, M., "Strain induced polarization chaos in a solitary VCSEL," Sci. Rep. **7**, 14032 (2017).
[58]Ramírez-Ávila, G. M., Jánosi, I. M., and Gallas, J. A. C., "Two-parameter areal scaling in the Hénon map," Europhys. Lett. **126**, 20001 (2019).
[59]Ramírez-Ávila, G. M., Kapitaniak, T., and Gonze, D., "Dynamical analysis of a periodically forced chaotic chemical oscillator," Chaos **34**, 073154 (2024).
[60]Ramírez-Ávila, G. M., Kurths, J., and Gallas, J. A. C., "Ubiquity of ring structures in the control space of complex oscillators," Chaos **31**, 101102 (2021).
[61]Ramírez-Ávila, G. M., Kurths, J., Gonze, D., and Dupont, G., "Exploring chronomodulated radiotherapy strategies in a chaotic population model," Chaos Soliton. Fract. **173**, 113743 (2023).
[62]Ramírez-Ávila, G. M., Muni, S. S., and Kapitaniak, T., "Unfolding the distribution of periodicity regions and diversity of chaotic attractors in the Chialvo neuron map," Chaos **34**, 083134 (2024).
[63]Rössler, O. E., "Equation for continuous chaos," Phys. Lett. A **57**, 397–398 (1976).
[64]San Miguel, M., Feng, Q., and Moloney, J. V., "Light-polarization dynamics in surface-emitting semiconductor lasers," Phys. Rev. A **52**, 1728–1739 (1995).
[65]Sciamanna, M., Gatare, I., Locquet, A., and Panajotov, K., "Polarization synchronization in unidirectionally coupled vertical-cavity surface-emitting lasers with orthogonal optical injection," Phys. Rev. E **75**, 056213 (2007).
[66]Sciamanna, M.and Panajotov, K., "Route to polarization switching induced by optical injection in vertical-cavity surface-emitting lasers," Phys. Rev. A **73**, 023811 (2006).
[67]Simpson, T. B., Liu, J. M., Gavrielides, A., Kovanis, V., and Alsing, P. M., "Period-doubling route to chaos in a semiconductor laser subject to optical injection," Appl. Phys. Lett. **64**, 3539–3541 (1994).
[68]Soda, H., Iga, K.-i., Kitahara, C., and Suematsu, Y., "GaInAsP/InP surface emitting injection lasers," Jpn. J. Appl. Phys. **18**, 2329 (1979).
[69]Torre, M., Hurtado, A., Quirce, A., Valle, A., Pesquera, L., and Adams, M., "Polarization switching in long-wavelength VCSELs subject to orthogonal optical injection," IEEE J. Quantum Electron. **47**, 92–99 (2011).
[70]Towe, E., Leheny, R. F., and Yang, A., "A historical perspective of the development of the vertical-cavity surface-emitting laser," IEEE J. Sel. Top. Quantum Electron. **6**, 1458–1464 (2000).
[71]Travagnin, M., "Linear anisotropies and polarization properties of vertical-cavity surface-emitting semiconductor lasers," Phys. Rev. A **56**, 4094–4105 (1997).
[72]Virte, M., Panajotov, K., Thienpont, H., and Sciamanna, M., "Deterministic polarization chaos from a laser diode," Nat. Photonics **7**, 60–65 (2013).
[73]Volos, C. K.and Gallas, J. A. C., "Experimental evidence of quint points and non-quantum chirality in a minimalist autonomous electronic oscillator," Eur. Phys. J. Plus **137**, 154 (2022).
[74]Wakao, K., Moriki, K., Kambayashi, T., and Iga, K., "GaInAsP/InP DH laser grown by newly designed vertical LPE furnace," Jpn. J. Appl. Phys. **16**, 2073 (1977).
[75]Wilmsen, C. W., Temkin, H., and Coldren, L. A., *Vertical-Cavity Surface-Emitting Lasers: Design, Fabrication, Applications* (Cambridge University Press, Cambridge, 2001).
[76]Wolf, A., Swift, J. B., Swinney, H. L., and Vastano, J. A., "Determining Lyapunov exponents from a time series," Physica D **16**, 285–317 (1985).
[77]Ziebell, L. F.and Gallas, J. A. C., "Stability of a Duffing oscillator with a position-dependent mass," Eur. Phys. J. Plus **138**, 930 (2023).
[78]Zou, Y., Donner, R. V., Donges, J. F., Marwan, N., and Kurths, J., "Identifying complex periodic windows in continuous-time dynamical systems using recurrence-based methods," Chaos **20**, 043130 (2010).
[79]Zou, Y., Marwan, N., Han, X., Donner, R. V., and Kurths, J., "Shrimp structure as a test bed for ordinal pattern measures," Chaos **34**, 123154 (2024).
[80]Zou, Y., Thiel, M., Romano, M. C., Kurths, J., and Bi, Q., "Shrimp structure and associated dynamics in parametrically excited oscillators," Int. J. Bifurcat. Chaos **16**, 3567–3579 (2006).